25. The OOMMF code is available at http://math.nist.gov/oommf.
26. A. J. Macdonald, P. C. Holdsworth, R. G. Melko, *J. Phys. Condens. Matter* **23**, 164208 (2011).
27. S. Ladak, D. Read, T. Tyliszczak, W. R. Branford, L. F. Cohen, *New J. Phys.* **13**, 023023 (2011).
28. E. Mengotti *et al.*, *Nat. Phys.* **7**, 68 (2011).
29. J. R. Williams, L. Dicarlo, C. M. Marcus, *Science* **317**, 638 (2007).
30. M. König *et al.*, *Science* **318**, 766 (2007).
31. D. Sherrington, S. Kirkpatrick, *Phys. Rev. Lett.* **35**, 1792 (1975).

Disentangling the Electronic and Phononic Glue in a High-T_c Superconductor

S. Dal Conte,[1]* C. Giannetti,[2,3]† G. Coslovich,[4]‡ F. Cilento,[4] D. Bossini,[3]§ T. Abebaw,[4]‖ F. Banfi,[2,3] G. Ferrini,[2,3] H. Eisaki,[5] M. Greven,[6] A. Damascelli,[7,8] D. van der Marel,[9] F. Parmigiani[4,10]

Unveiling the nature of the bosonic excitations that mediate the formation of Cooper pairs is a key issue for understanding unconventional superconductivity. A fundamental step toward this goal would be to identify the relative weight of the electronic and phononic contributions to the overall frequency (Ω)–dependent bosonic function, $\Pi(\Omega)$. We performed optical spectroscopy on $Bi_2Sr_2Ca_{0.92}Y_{0.08}Cu_2O_{8+\delta}$ crystals with simultaneous time and frequency resolution; this technique allowed us to disentangle the electronic and phononic contributions by their different temporal evolution. The spectral distribution of the electronic excitations and the strength of their interaction with fermionic quasiparticles fully account for the high critical temperature of the superconducting phase transition.

Lattice vibrations (*1*) and excitations of electronic origin, such as spin or electric polarizability fluctuations (*2*) and loop currents (*3*), are generally considered potential mediators of Cooper pairing in the copper oxide high-temperature superconductors (cuprates). The generic interaction of fermionic quasi-particles (QPs) with bosonic excitations is accounted for by the bosonic function $\Pi(\Omega)$ [usually indicated as $\alpha^2 F(\Omega)$ for phonons and $I^2\chi(\Omega)$ for spin fluctuations], a dimensionless function that depends on the density of states of the excitations and the strength of their coupling to QPs. Because both the energy dispersion and lifetime of QPs are strongly affected by the interactions, signatures of QP-boson coupling have been observed in experiments that probe the electronic properties at equilibrium. The ubiquitous kinks in the QP dispersion at ~70 meV, measured by angle-resolved photoemission spectroscopy (ARPES) (*4*), have been interpreted in terms of coupling to either optical Cu-O lattice modes (*5, 6*) or spin excitations (*7*). Inelastic neutron and x-ray scattering experiments found evidence for both QP-phonon anomalies (*8*) and bosonic excitations attributed to spin fluctuations (*7, 9*) and loop currents (*10*). Dip features in tunneling experiments have been used to alternatively support the scenarios of dominant electron-phonon interactions (*11*) or antiferromagnetic spin fluctuations (*12*). The frequency-dependent dissipation of the Drude optical conductivity, $\sigma(\omega)$, measured by equilibrium optical spectroscopies, has been interpreted (*13–15*) as the coupling of electrons to bosonic

excitations, in which the separation of the phononic and electronic contributions is impeded by their partial coexistence on the same energy scale (<90 meV).

We have disentangled the electronic and phononic contributions to $\Pi(\Omega)$ through a non-equilibrium optical spectroscopy, in which femtosecond time resolution is combined with an energy resolution smaller than 10 meV over a wide photon energy range (0.5 to 2 eV). Our approach can be rationalized on the basis of the widely used assumption (*16, 17*) that, after the interaction between a superconductor and a short laser pulse (1.55 eV photon energy), the effective electronic temperature (T_e) relaxes toward its equilibrium value through energy exchange with the different degrees of freedom that linearly contribute to $\Pi(\Omega)$. In a more formal description, the total bosonic function is given by

$$\Pi(\Omega) = \Pi_{be}(\Omega) + \Pi_{SCP}(\Omega) + \Pi_{lat}(\Omega) \quad (1)$$

where Π_{be} refers to the bosonic excitations of electronic origin at the effective temperature T_{be}, Π_{SCP} to the small fraction of strongly coupled phonons (SCPs) at T_{SCP} (*16*), and Π_{lat} to all other lattice vibrations at T_{lat}. Because the term that couples the rate equations (*18*) for T_e and T_b (with b = be, SCP, lat) is $G(\Pi_b, T_b, T_e)/C_b$ [where G is the functional described in (*18*) and C_b is the specific heat of the bosonic population], each subset of the bosonic excitations is characterized by different relaxation dynamics on the femtosecond time scale. The most convenient systems for such an experiment are the hole-doped cuprates close to the optimal dopant concentration needed to attain the maximum critical temperature T_c, in which the total $\Pi(\Omega)$ is maximum (*15*). Despite the magnitude of $\Pi(\Omega)$, vertex corrections beyond

[1]Department of Physics A. Volta, Università degli Studi di Pavia, Pavia I-27100, Italy. [2]I-LAMP (Interdisciplinary Laboratories for Advanced Materials Physics), Università Cattolica del Sacro Cuore, Brescia I-25121, Italy. [3]Department of Physics, Università Cattolica del Sacro Cuore, Brescia I-25121, Italy. [4]Department of Physics, Università degli Studi di Trieste, Trieste I-34127, Italy. [5]Nanoelectronics Research Institute, National Institute of Advanced Industrial Science and Technology, Tsukuba, Ibaraki 305-8568, Japan. [6]School of Physics and Astronomy, University of Minnesota, Minneapolis, MN 55455, USA. [7]Department of Physics and Astronomy, University of British Columbia, Vancouver, BC V6T 1Z1, Canada. [8]Quantum Matter Institute, University of British Columbia, Vancouver, BC V6T 1Z4, Canada. [9]Département de Physique de la Matière Condensée, Université de Genève, Genève CH1211, Switzerland. [10]Sincrotrone Trieste S.C.p.A., Basovizza I-34012, Italy.

*Present address: Physics Department, Eindhoven University of Technology, 5600 MB Eindhoven, Netherlands.
†To whom correspondence should be addressed. E-mail: claudio.giannetti@unicatt.it
‡Present address: Materials Sciences Division, Lawrence Berkeley National Laboratory, Berkeley, CA 94720, USA.
§Present address: Institute for Molecules and Materials, Radboud University Nijmegen, 6525 AJ Nijmegen, Netherlands.
‖Present address: Zernike Institute for Advanced Materials, University of Groningen, NL-9700 AG Groningen, Netherlands.

Fig. 1. Nonequilibrium reflectivity. The relative reflectivity variation $\delta R/R(\omega, T) = [R(\omega, T + \delta T) - R(\omega, T)]/R$, calculated for the incremental variations δT_e and δT_b in Eqs. 2 and 3 and using the $\Pi(\omega)$ value obtained from the fit to the equilibrium measurements, is reported. The change of sign of $\delta R(\omega, T)/R$ in the quasi-thermal scenario (gray line; $\delta T_e = \delta T_b = 1$ K) and the maximum $\delta R(\omega, T)/R$ in the non-thermal scenario (red line; $\delta T_e = 5$ K, $\delta T_b = 0$) occur at a frequency coinciding with the dressed plasma frequency, $\Omega_p \sim 1$ eV. The spectral regions probed by the optical parametric amplifier (OPA) and supercontinuum techniques (*18*) are indicated.
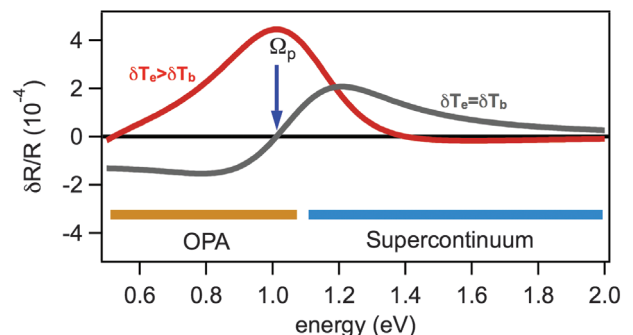
Eliashberg theory can be reliably neglected (9, 15) in this doping regime.

The total bosonic function $\Pi(\Omega)$ is directly determined by fitting an extended Drude model (18) and a sum of Lorentz oscillators accounting for the interband optical transitions in the visible region (19) to the equilibrium dielectric function of optimally doped $Bi_2Sr_2Ca_{0.92}Y_{0.08}Cu_2O_{8+\delta}$ (Y-Bi2212) high-quality crystals (20) (T_c = 96 K) measured at T = 300 K by conventional spectroscopic ellipsometry (21). If we assume a histogram-like form (18) (fig. S1) and impose an upper limit of 1 eV, the extracted $\Pi(\Omega)$ is characterized by (i) a low-energy part (up to 40 meV) compatible with the coupling to acoustic phonons (22) and Raman-active optical phonons involving c-axis motion of the Cu ions (23); (ii) a narrow, intense peak centered at ~60 meV, attributed to the anisotropic coupling to either out-of-plane buckling and in-plane breathing Cu-O optical modes (6) or bosonic excitations of electronic origin such as spin fluctuations (7); and (iii) a broad continuum extending up to 350 meV (13–15), well above the characteristic phonon cutoff frequency (~90 meV).

The key point to extend this analysis to nonequilibrium experiments is that the electron self-energy, $\Sigma(\omega, t)$, used to calculate $\sigma(\omega, t)$ (18), can be factorized into

$$\Sigma(\omega, T) = \int_0^\infty \Pi(\Omega) L(\omega, \Omega, T) d\Omega \quad (2)$$

(24), where $L(\omega, \Omega, T)$ is a material-independent kernel function accounting for the thermal activation of the bosonic excitations and of the QPs. The kernel function is given by

$$L(\omega, \Omega, T_{e,b}) = -2\pi i \left[N(\Omega, T_b) + \frac{1}{2} \right] +$$
$$\Psi\left[\frac{1}{2} + \frac{i(\Omega - \Omega')}{2\pi T_e} \right] - \Psi\left[\frac{1}{2} - \frac{i(\Omega + \Omega')}{2\pi T_e} \right]$$
$$(3)$$

where Ψ is the digamma function obtained by integrating the Fermi-Dirac functions, and $N(\Omega, T_b)$ is the Bose distribution at temperature T_b. The kernel function can be decomposed into different terms depending on the electronic (T_e) and bosonic (T_b) temperatures. The independent variation of $T_{e,b}$ is expected to induce different modifications of the dielectric function. Figure 1 shows the expected relative variation of the reflectivity, expressed as

$$\frac{\delta R}{R}(\omega, T) = \frac{R(\omega, T + \delta T) - R(\omega, T)}{R(\omega, T)} \quad (4)$$

in the quasi-thermal ($\delta T_e = \delta T_b > 0$) and nonthermal ($\delta T_e > 0$, $\delta T_b = 0$) scenarios. Phenomenologically, in the first case the reflectivity variation is dominated by the increase of the QP-boson scattering, corresponding to a broadening of the Drude peak, whereas in the second case the decoupling between the QP and bosonic distributions can be rationalized in terms of a small increase of the plasma frequency without any change in the scattering rate. The difference between the two cases is more evident in the spectral region close to the dressed plasma frequency, $\Omega_p \approx 1$ eV—that is, an energy scale much higher than the energy scale of the bosonic function.

Time-resolved reflectivity measurements in the 0.5 to 2 eV photon-energy range (25) have been performed at T = 300 K on the same crystals (20) (OP96) used for the equilibrium optical spectroscopy. The $\delta R/R(\omega, t)$ two-dimensional matrix is reported in Fig. 2, A and B, along with the time traces at ~1.5 and 0.7 eV photon energies (white curves). After the pump excitation at $t = 0$, the temporal dynamics above and below Ω_p are very similar, exhibiting a relaxation dynamics of about 200 fs, generally attributed to the thermalization of electrons with SCPs (16), and a slower decay on the picosecond time scale, related to the thermalization with all other lattice vibrations. Shown in Fig. 2C are the energy-resolved traces at fixed delay (t = 100 fs). Comparing the $\delta R/R(\omega)$ measured on OP96 to the relative variation of the reflectivity calculated in the nonthermal and quasi-thermal cases (Fig. 1), we come to the major point of our work: The electrons thermalize with part of the bosonic excitations, described by $\Pi(\Omega)$, on a time scale faster than the electron-phonon thermalization. The fast time scale (<<100 fs) of this thermalization implies a very large coupling and a relatively small specific heat. These overall observations strongly suggest that this process involves bosonic excitations of electronic origin.

The relative strengths of $\Pi_b(\Omega)$ (where the index b refers to the three components in Eq. 1) determine (26) both the temporal evolution of the temperatures T_b, through the four-temperature model (4TM) (18), and the intensity of the reflectivity variation, through Eq. 2. As a consequence, the simultaneous fit of the calculated $\delta R/R(\omega, T_e, T_{be}, T_{SCP}, T_{lat})$ to the data reported in Fig. 2 in the time and frequency domain decisively narrows the phase space of the parameters of the model, as compared to single-color measurements. The fit procedure (18) allows
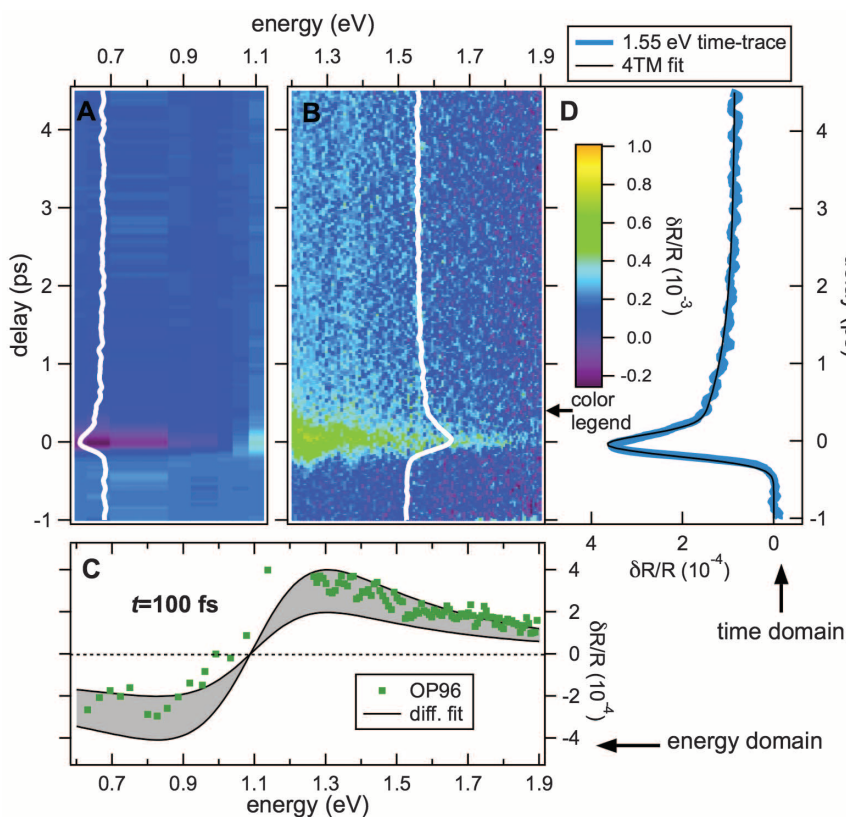
Fig. 2. Nonequilibrium optical spectroscopy. (**A** and **B**) Time- and frequency-resolved reflectivity measurements carried out on the OP96 sample at T = 300 K in the OPA (A) and supercontinuum (B) probe optical region (18). The white curves represent the time traces at photon energies of 1.55 eV and 0.65 eV, respectively. (**C**) Energy-resolved spectra for OP96, measured at fixed time t = 100 fs. The black lines are the maximum and minimum $\delta R/R(\omega, t = 100$ fs) determined through the fitting procedure described in the text and in (18) and accounting for the experimental uncertainty in the laser fluence and spot dimensions. Most of the values of $\delta R/R(t = 100$ fs) measured on OP96 at each wavelength fall between the two lines. (**D**) Time-resolved trace for OP96 at fixed photon energy of 1.55 eV. The black line is the best fit to the data obtained through the fitting procedure described in (18).

Fig. 3. Disentangling the contributions to the total bosonic function. The electronic (Π_{be}, red areas), strongly coupled phonon (Π_{SCP}, blue area), and lattice (Π_{lat}, green area) contributions to the total bosonic function are shown. The insets display the temporal evolution of the temperatures T_{be} (red line), T_{SCP} (blue line), and T_{lat} (green line) determined through the 4TM (18). Sketches of the possible microscopic mechanisms at the base of the different contributions to the total $\Pi(\Omega)$ are shown in the upper panels.
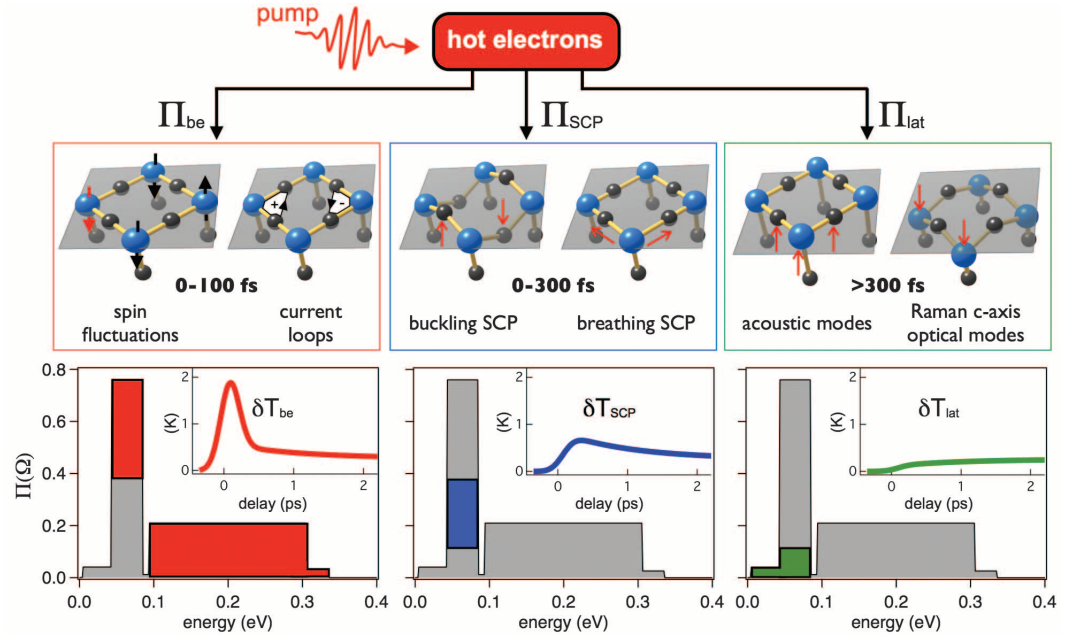
us to unambiguously extract the different contributions to $\Pi(\Omega)$ and to estimate C_{be} and C_{SCP}.

Figure 3 summarizes the main results of this work. The pump pulse of 10 μJ/cm^2 gently increases the electronic temperature by $\delta T_e \sim 2$ K. The entire high-energy part and ~46% of the peak (red areas) instantaneously thermalize with electrons at a temperature $T_{be} \approx T_e$. The spectral distribution and the value of the specific heat of these excitations ($C_{be} < 0.1 C_e$) demonstrate their electronic origin. On a slower time scale (100 to 200 fs), the electrons thermalize with the SCPs that represent ~20% of the phonon density of states ($C_{SCP} = 0.2 C_{lat}$) but are responsible for ~34% of the coupling (blue area) in the peak of the bosonic function at 40 to 75 meV, corresponding to ~17% of the total bosonic function. Prominent candidates as SCPs are the buckling and breathing Cu-O optical modes. The third and last measured time scale is related to the thermalization with all other lattice modes (80% of the total), which include all acoustic modes and the infrared- and Raman-active modes involving c-axis motion of the Cu ions and provide less than 20% of the coupling (green area) in the peak of $\Pi(\Omega)$.

These results have important implications for the identification of the pairing mechanism in cuprates. The electron-boson coupling $\lambda_b = 2\int \Pi_b(\Omega)/\Omega \ d\Omega$ is calculated for each subset b of the bosonic excitations, considering the experimental uncertainties. In the strong-coupling regime ($\lambda_b < 1.5$), the critical temperature can be estimated (18) through an extended version of McMillan's equation (27), containing the logarithmic-averaged frequency ($\tilde{\Omega}$) and the portion of $\Pi_b(\Omega)$ that contributes to the d-wave pairing (28). The maximal critical temperature attainable is calculated assuming that each $\Pi_b(\Omega)$ entirely contributes to the d-wave pairing. The

coupling with SCPs ($\lambda_{SCP} = 0.4 \pm 0.2$) is in complete agreement with the values measured on similar materials via different techniques, such as time-resolved photoemission spectroscopy (16), time-resolved electron diffraction (17), and single-color high-resolution time-resolved reflectivity (29). Although this value is rather close to the threshold of the strong-coupling regime (30, 31), the small value of $\tilde{\Omega}$ gives $T_c = 2$ to 30 K, which is far from being able to account for the high-temperature superconductivity of the system. The coupling of electrons with all other lattice vibrations is even smaller in strength ($\lambda_{lat} = 0.2 \pm 0.2$) and provides an upper bound of the critical temperature of $T_c \approx 12$ K. Finally, the large coupling constant ($\lambda_{be} = 1.1 \pm 0.2$) and the larger $\tilde{\Omega}$ value of the electronic excitations give $T_c = 105$ to 135 K, and this alone accounts for the high critical temperature. We note that, whereas $\Pi_{SCP}(\Omega)$ and $\Pi_{lat}(\Omega)$ are expected to be temperature-independent, $\Pi_{be}(\Omega)$ increases as new magnetic excitations emerge when approaching T_c, particularly in the pseudogap phase (10). Therefore, the use of $\Pi_{be}(\Omega)$ determined at $T = 300$ K to estimate the QP-boson coupling and T_c underestimates the electronic contribution to the pairing, further supporting our conclusion of a dominant electronic mechanism in the superconductivity of cuprates. All the λ_b values, maximum attainable critical temperatures, and important parameters for each subset of the total bosonic function are reported in table S1.

The measured values of λ_{be}, λ_{SCP}, and λ_{lat} and the spectral distribution of the bosonic excitations strongly indicate that the antiferromagnetic spin fluctuations (7, 9) and the loop currents (3) are the most probable mediators for the formation of Cooper pairs. An isotope effect in the dispersion of nodal QPs has been observed by ARPES measurements on optimally doped Bi2212

(32). Analysis of these data (33) indicates that the nodal isotope effect can be explained by assuming that the QP-phonon coupling represents about 10% of the total contribution of other bosonic excitations. From Fig. 3, we estimate that the contribution of SCP is less than 20% of the total bosonic function. Hence, our results fully explain the observed isotope effect, providing a consistent interpretation of the most important experimental results about the QP-boson coupling in cuprates.

Our conclusions are rather independent of the assumption of the histogram-like form of $\Pi(\Omega)$ and are robust against modifications of the details of the equilibrium dielectric function. In fact, the outcome of this work strongly supports the factorization of the self-energy at $T = 300$ K into a temperature-dependent kernel function and the glue function $\Pi(\Omega)$ (see Eq. 2), even under nonequilibrium conditions. Although we do not exclude a priori that the upper limit used in the determination of the bosonic function can hide possible contributions to $\Pi(\Omega)$ even above 1 eV and that the electron-phonon coupling may cooperate in driving the superconducting phase transition, we demonstrate that bosonic excitations of electronic origin are the most important factor in the formation of the superconducting state at high temperatures in the cuprates. Our findings pave the way for the investigation of electron-boson coupling in a variety of complex materials, such as transition-metal oxides and iron-based superconductors.

References and Notes
1. V. Kresin, S. Wolf, *Rev. Mod. Phys.* **81**, 481 (2009).
2. P. Monthoux, D. Pines, G. G. Lonzarich, *Nature* **450**, 1177 (2007).
3. C. Varma, *Phys. Rev. B* **73**, 155113 (2006).
4. A. Damascelli, Z. Hussain, Z.-X. Shen, *Rev. Mod. Phys.* **75**, 473 (2003).

5. A. Lanzara et al., Nature 412, 510 (2001).
6. T. P. Devereaux, T. Cuk, Z.-X. Shen, N. Nagaosa, Phys. Rev. Lett. 93, 117004 (2004).
7. T. Dahm et al., Nat. Phys. 5, 217 (2009).
8. D. Reznik et al., Nature 440, 1170 (2006).
9. M. Le Tacon et al., Nat. Phys. 7, 725 (2011).
10. Y. Li et al., Nature 468, 283 (2010).
11. J. Lee et al., Nature 442, 546 (2006).
12. O. Ahmadi, L. Coffey, J. F. Zasadzinski, N. Miyakawa, L. Ozyuzer, Phys. Rev. Lett. 106, 167005 (2011).
13. M. Norman, A. Chubukov, Phys. Rev. B 73, 140501 (2006).
14. J. Hwang, T. Timusk, E. Schachinger, J. Carbotte, Phys. Rev. B 75, 144508 (2007).
15. E. van Heumen et al., Phys. Rev. B 79, 184512 (2009).
16. L. Perfetti et al., Phys. Rev. Lett. 99, 197001 (2007).
17. F. Carbone, D.-S. Yang, E. Giannini, A. H. Zewail, Proc. Natl. Acad. Sci. U.S.A. 105, 20161 (2008).
18. See supporting material on Science Online.
19. C. Giannetti et al., Nat. Commun. 2, 353 (2011).
20. H. Eisaki et al., Phys. Rev. B 69, 064512 (2004).
21. D. van der Marel et al., Nature 425, 271 (2003).
22. S. Johnston et al., http://arxiv.org/pdf/1101.1302.pdf (2011).
23. N. Kovaleva et al., Phys. Rev. B 69, 054511 (2004).
24. H. J. Kaufmann, E. G. Maksimov, E. K. H. Salje, J. Superconduct. 22, 755 (1998).
25. F. Cilento et al., Appl. Phys. Lett. 96, 021102 (2010).
26. P. B. Allen, Phys. Rev. Lett. 59, 1460 (1987).
27. P. B. Allen, R. Dynes, Phys. Rev. B 12, 905 (1975).
28. A. J. Millis, S. Sachdev, C. M. Varma, Phys. Rev. B 37, 4975 (1988).
29. C. Gadermaier et al., Phys. Rev. Lett. 105, 257001 (2010).
30. A. S. Mishchenko, N. Nagaosa, Phys. Rev. Lett. 93, 036402 (2004).
31. G. Sangiovanni, O. Gunnarsson, E. Koch, C. Castellani, M. Capone, Phys. Rev. Lett. 97, 046404 (2006).
32. H. Iwasawa et al., Phys. Rev. Lett. 101, 157005 (2008).
33. E. Schachinger, J. Carbotte, T. Timusk, Europhys. Lett. 86, 67003 (2009).

Coherent Sensing of a Mechanical Resonator with a Single-Spin Qubit

Shimon Kolkowitz,[1]* Ania C. Bleszynski Jayich,[2] Quirin P. Unterreithmeier,[1]*
Steven D. Bennett,[1] Peter Rabl,[3] J. G. E. Harris,[4] Mikhail D. Lukin[1]†

Mechanical systems can be influenced by a wide variety of small forces, ranging from gravitational to optical, electrical, and magnetic. When mechanical resonators are scaled down to nanometer-scale dimensions, these forces can be harnessed to enable coupling to individual quantum systems. We demonstrate that the coherent evolution of a single electronic spin associated with a nitrogen vacancy center in diamond can be coupled to the motion of a magnetized mechanical resonator. Coherent manipulation of the spin is used to sense driven and Brownian motion of the resonator under ambient conditions with a precision below 6 picometers. With future improvements, this technique could be used to detect mechanical zero-point fluctuations, realize strong spin-phonon coupling at a single quantum level, and implement quantum spin transducers.

Hybrid quantum systems offer many potential applications in quantum information science and quantum metrology. One example is cavity quantum electrodynamics (cQED), in which a quantum two-level system (a qubit) is strongly coupled to resonant photons in an electromagnetic cavity (1–3). In the mechanical analog of cQED, the qubit is coupled to a mechanical resonator, with resonant phonons playing the role of cavity photons (4–7). Mechanical resonators are promising components for hybrid quantum systems because they couple to a wide range of forces while maintaining high quality factors (8–13) and can be fabricated using scalable techniques. A recent experiment demonstrated coupling of a superconducting phase qubit to the quantum motion of a piezoelectric resonator at millikelvin temperatures (11). However, this approach resulted in relatively short phonon lifetimes and is not easily extended to other resonator-qubit systems. An important goal is to extend this technique to nonpiezoelectric resonators that offer longer phonon lifetimes and to qubits featuring longer coherence times (4, 5, 9, 10, 14, 15). In particular, spin states of localized atomlike systems in the solid state can be manipulated individually and can serve as an exceptional quantum memory, even under ambient conditions. Moreover, experiments have demonstrated that resonators can be sensitive to the magnetic force associated with a single electronic spin (16). Control over a coupled spin-resonator hybrid quantum system could be used to mediate long-range spin-spin coupling for quantum information applications (17) or to manipulate mechanical motion at the single quantum level with long qubit and phonon coherence times (4, 11). In addition, coherent control over spin-phonon interactions is of direct relevance for realizations of novel nanoscale sensors (18–20).

In our experiment (Fig. 1A), we used the electronic spin associated with an individual nitrogen vacancy (NV) center to sense the motion of a nearby, magnetized atomic force microscopy (AFM) cantilever. The time-varying magnetic field generated by the displacement of the magnetic tip coherently drives the qubit evolution, which is subsequently detected via optical spin measurements. The essence of our approach (Fig. 1B) is to synchronize the evolution of the single spin with the cantilever's oscillations. When the spin is driven by a pulse train with a period matching the mechanical period, the motion constructively affects the spin evolution over a long interaction time, enhancing the spin's sensitivity in a narrow frequency band (21). In addition, the pulses dynamically decouple the NV spin from the slow evolution of the surrounding environment, increasing the possible interrogation time (22, 23).

The NV centers are implanted ~5 nm below the surface of a bulk diamond sample. The spin sublevels $|m_s = 0\rangle$ and $|m_s = \pm 1\rangle$ of the electronic ground state exhibit a zero-field splitting of ~2.87 GHz. In the presence of a static magnetic field, the degeneracy between $|+1\rangle$ and $|-1\rangle$ is lifted, allowing us to selectively address the $|0\rangle \rightarrow |+1\rangle$ transition with microwave radiation. The magnetic field $\mathbf{B_{tip}}$ generated by the tip at the position of the NV results in an additional Zeeman shift of the splitting, given by $\Delta\omega = g_e \mu_B \mathbf{B_{tip}} \cdot \hat{\mathbf{z}}/\hbar$, where $g_e \simeq 2$ is the electron g-factor, μ_B is the Bohr magneton, $\hbar$ is Planck's constant divided by 2π, and $\hat{\mathbf{z}}$ is the unit vector along the NV axis. With the tip held at a constant position, the static Zeeman shift is detected by performing continuous wave (CW) electron spin resonance (ESR) measurements (Fig. 1C). By scanning the tip at a fixed height above the diamond surface with a piezoelectric scanning stage and monitoring $\Delta\omega$, we mapped the projection of $\mathbf{B_{tip}}$ along the NV axis (Fig. 1D). This provides an accurate measurement of the magnetic field gradient G_m produced by the tip along the NV axis, which

[1]Department of Physics, Harvard University, Cambridge, MA 02138, USA. [2]Department of Physics, University of California Santa Barbara, Santa Barbara, CA, USA. [3]Institute for Quantum Optics and Quantum Information of the Austrian Academy of Science, 6020 Innsbruck, Austria. [4]Departments of Physics and Applied Physics, Yale University, New Haven, CT, USA.

*These authors contributed equally to this work.
†To whom correspondence should be addressed. E-mail: lukin@physics.harvard.edu